

Oxide/Halide/Oxide Architecture for High Performance Semi-Transparent Perovskite Solar Cells

Min Ju Jeong, Jun Hyeok Lee, Chang Hyuk You, So Yeon Kim, Seungmin Lee, and Jun Hong Noh*

A device architecture with n-type oxide/perovskite halide/p-type oxide for the sputtering damage-free semi-transparent perovskite solar cells (PSCs) is reported. A p-type nickel oxide (NiO_x) nanoparticle overlayer on a perovskite layer is introduced to act as both a hole transporting layer and buffer layer to avoid sputtering damage during deposition of transparent conducting oxide. The NiO_x based semi-transparent PSCs exhibit superior durability under harsh sputtering conditions such as high temperature and sputtering power, enabling the high quality of transparent electrodes. With optimal sputtering condition for tin-doped indium oxide (ITO) as a top transparent electrode, the semi-transparent device shows an enhanced power conversion efficiency (PCE) of 19.5% (20.5% with a back reflector), which is higher than that of the opaque device (19.2%). The semi-transparent devices also shows superior storage stability without encapsulation under 10% relative humidity, retaining over 90% of initial PCE for 1000 h. By controlling the molar concentration of perovskite solution, a semi-transparent PSC with a PCE of 12.8%, showing a high average visible transmittance (AVT) of 30.3%, is fabricated. The authors believe that this architecture with n-type oxide/perovskite halide/p-type oxide represents a cornerstone for the high performance and commercialization of semi-transparent PSCs.

absorption coefficients, long carrier diffusion lengths, and easily tunable band gaps.^[4–7] Furthermore, PSCs have advantages such as a cost-effective fabrication process, low cost of materials, and high power conversion efficiency (PCE) over 25%.^[8–16] These advantages make PSCs a highly promising candidate for semi-transparent solar cells.

To date, various transparent electrodes such as indium tin oxide (ITO), indium zinc oxide (IZO), indium zinc tin oxide (IZTO), ultrathin metal layer, and oxide/metal/oxide (OMO) structure have been used to fabricate the top transparent electrodes (TTEs) of semi-transparent PSCs through a vacuum or solution process.^[17–25] Among the deposition processes, the transparent electrode fabricated by the solution process is not only chemically unstable but also not good in terms of reproducibility.^[17,26] In contrast, the sputtering process is a mature large-area coating technology at present, and it is excellent in terms of chemical stability and reproducibility.^[27,28] Therefore,

transparent conducting oxides (TCOs) manufactured via the sputtering process are suitable for large-area semi-transparent PSCs. In the case of the sputtering process on the glass for the bottom transparent electrodes (BTEs), there are no limitations of the sputtering conditions such as the temperature, sputtering power, and working pressure. However, in the case of the deposition for TTEs, energetic particles such as reflected Ar, negative oxygen ions, and neutral particles bombard with underlying organic or perovskite layer during the sputtering process, resulting in the degradation of the photovoltaic performance of semi-transparent PSCs.^[29,30] Therefore, introducing a buffer layer is required to prevent sputtering damages during the deposition of TTEs.

Conventional semi-transparent PSCs are fabricated using a buffer layer, which prevents sputtering damage to organic hole transport layers (HTLs) such as 2,2',7,7'-tetrakis[N,N-di(4-methoxyphenyl)amino]-9,90-spirobifluorene (spiro-OMeTAD) and poly(triaryl)amine (PTAA) during the deposition of TTEs.^[20,31] Molybdenum oxide (MoO_x) has been commonly used as a buffer layer in semi-transparent PSCs.^[23,32] However, MoO_x has poor thermal stability and induces parasitic absorption, which deteriorates the performance of semi-transparent

1. Introduction

Semi-transparent solar cells have attracted enormous attention owing to numerous photovoltaic applications such as tandem photovoltaics, building integrated photovoltaics (BIPV), and smart windows.^[1–3] Halide perovskite solar cell (PSC) is an ideal candidate for semi-transparent solar cells due to the excellent optoelectronic properties of halide perovskites, including high

M. J. Jeong, J. H. Lee, C. H. You, S. Y. Kim, S. Lee, J. H. Noh
School of Civil

Environmental and Architectural Engineering
Korea University
Seoul 02841, Republic of Korea
E-mail: junhnoh@korea.ac.kr

J. H. Noh
KU-KIST Green School Graduate School of Energy and Environment
Korea University
Seoul 02841, Republic of Korea

 The ORCID identification number(s) for the author(s) of this article can be found under <https://doi.org/10.1002/aenm.202200661>.

DOI: 10.1002/aenm.202200661

PSCs.^[33–35] Furthermore, the usage of a buffer layer for semi-transparent PSCs increases the number of process steps and the production costs, acting as obstacles for commercialization. It is crucial to fabricate the semi-transparent PSCs without a buffer layer in terms of commercialization. Therefore, charge transporting layers (CTLs), which not only transfer charges but also resist the sputtering damages, are required for the commercialization of semi-transparent PSCs. Oxide CTLs are thermally stable as well as physically durable, thereby enabling to prevent sputtering damages.^[30] Therefore, a promising semi-transparent PSC structure is the BTE/n-type oxide/perovskite halide/p-type oxide/TTE structure without a buffer layer. The p-type oxide layer on the perovskite layer acts as a p-type CTL as well as a buffer layer.

Herein, we report sputtering damage-free semi-transparent PSCs with the n-i-p structure, which is composed of TCO/n-type oxide/perovskite/p-type oxide/TCO without a buffer layer. We introduced nickel oxide (NiO_x) as a p-type oxide layer to act as a hole extraction layer as well as to prevent sputtering damage during ITO deposition. We confirmed the NiO_x nanoparticles (NPs) layer on the perovskite layer effectively prevents sputtering damage even under harsh deposition conditions such as high temperature and sputtering power. Therefore, we were able to fabricate excellent quality ITO films on the NiO_x layer by applying high sputtering power, enabling us to produce ITO films with improved conductivity and transmittance. Compared with opaque PSCs with Au as a top electrode, semi-transparent PSCs with ITO showed a higher PCE of 19.5% (20.5% with a back reflector), which is the highest value among reported organic-free semi-transparent PSCs thus far. Additionally, the semi-transparent devices maintained over 90% of the initial PCE for 1000 h under 10% relative humidity without any encapsulation. Furthermore, we achieved an average visible transmittance (AVT) of 30.31% for the semi-transparent device by controlling the molar concentration of the perovskite solution. We believe that this optimal device architecture with TCO/oxide/perovskite/oxide/TCO provides a novel route for achieving high-performance semi-transparent PSCs.

2. Results and Discussions

Figure 1a exhibits a schematic illustration of the mechanism for damage-free semi-transparent PSCs during the sputtering process. There are three conditions: i) a perovskite layer without any upper layer; ii) organic CTLs on the perovskite layer; and iii) metal oxide CTLs on the perovskite layer. Without any protective layer on the perovskite layer during the sputtering process, energetic particles break down the perovskite structure and induce decomposition to PbI₂, which adversely affects the operation of the device.^[18,30] With organic CTLs on the perovskite layer, organic CTLs not only are damaged by bombardment with the energetic particles but also do not protect the perovskite layer.^[36,37] On the other hand, in the case of metal oxide CTLs on the perovskite layer, it is possible to prevent sputtering damage without a buffer layer, maintaining the photovoltaic performance of the device. Therefore, the metal oxide CTLs on top of the perovskite layer is the optimal condition to fabricate semi-transparent PSCs without sputtering damage.

To fabricate the sputtering damage-free semi-transparent PSCs, we synthesized ligand-off NiO_x as the metal oxide CTL according to a previously reported method (Figure 1b).^[38] Figure 1c shows the transmission electron microscopy (TEM) image of synthesized NiO_x NPs, which show a uniform particle size without agglomeration. To coat the ligand-off NiO_x NPs onto the perovskite layer without damage, NiO_x NPs should be dispersed in non-polar solvents such as toluene, chlorobenzene and long-chain alcohols. To disperse NiO_x in a non-polar solvent, we used the Hansen solubility parameter (HSP) theory, which is a powerful tool that enables theoretical prediction of the dispersibility of NPs in a solvent system.^[38] HSP theory is used to explain the interaction between solute and solvent by three parameters (dispersive interactions of δ_d , polar interactions of δ_p , hydrogen bonding of δ_h). The Hansen distance (R_a) is calculated by following Equation (1), where subscripts 1 and 2 represent the NPs and the solvent, respectively:

$$R_a^2 = 4(\delta_{d,2} - \delta_{d,1})^2 + (\delta_{p,2} - \delta_{p,1})^2 + (\delta_{h,2} - \delta_{h,1})^2 \quad (1)$$

The calculated HSPs of NiO_x NPs for δ_d , δ_p and δ_h are 16.9, 7.0 and 9.3 MPa^{1/2}, respectively, and the interaction radius (R_0) is 4 MPa^{1/2}. According to the calculated results, Figure 1d represents the interaction sphere of NiO_x NPs, which indicates the dispersibility of NiO_x NPs in a certain solvent. It is found that 1-hexanol (HxOH) is located inside of the sphere, indicating the good solvent for dispersion of NiO_x NPs. We confirmed that NiO_x NPs are well dispersed in HxOH, as shown in the Figure 1d inset photograph.

To investigate the function of HxOH for NiO_x NPs solvent, we conducted XRD analysis for the perovskite films after surface treatment with HxOH, ethanol (EtOH), methanol (MtOH), and isopropanol (IPA), respectively. As shown in Figure S1a, Supporting Information, perovskite films treated with MtOH, EtOH, and IPA showed a PbI₂ peak, which suggests decomposition of the perovskite films. To further investigate the damage to perovskite film by solvents, we submerged the perovskite films in HxOH, MtOH, EtOH, and IPA for 5 min (Figure S1b, Supporting Information). Except for the HxOH, we observed decomposition of perovskite films in MtOH, EtOH, and IPA. This result indicates that HxOH does not damage the perovskite film. We also conducted HSP analysis of HxOH, EtOH, MtOH, and IPA for the NiO_x NPs dispersion. As shown in Figure S2a, Supporting Information, MtOH, EtOH and IPA were located outside the sphere except for HxOH, indicating that MtOH, EtOH and IPA are not suitable solvents for dispersing NiO_x NPs. As shown in Figure S2b, Supporting Information, NiO_x NPs were well dispersed in HxOH solvent, but not in other solvents. These results suggest that HxOH is a suitable solvent for NiO_x NPs dispersion.

To investigate the NiO_x NPs concentration in HxOH that is required to cover the perovskite films completely, we conducted scanning electron microscopy (SEM) measurements of the NiO_x films with different concentrations of NiO_x solution (Figure 1e–j). A uniform and compact NiO_x layer on the perovskite layer is formed at a concentration of 30 mg mL^{−1}, while the NiO_x NPs did not completely cover the perovskite layer at a concentration of 20 mg mL^{−1} or less. A concentration of 30 mg mL^{−1} or more is required for fabricating semi-transparent PSCs.

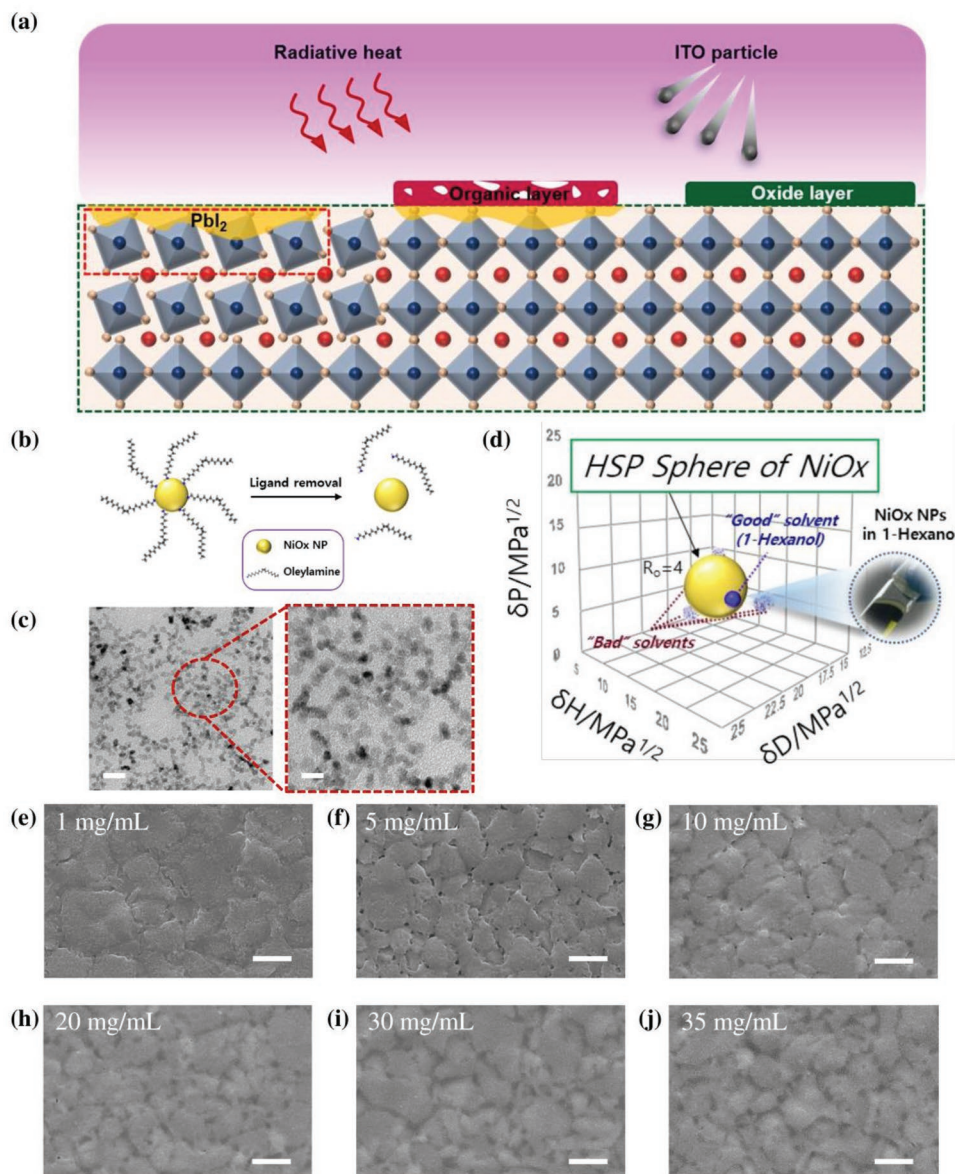


Figure 1. a) A schematic illustration of the mechanism for damage-free semi-transparent perovskite solar cells. b) Ligand-free NiO_x particle after ligand removal. c) Transmission electron microscopy (TEM) image of NiO_x. Left is low magnification, right is high magnification. Scale bar, 20 nm. d) Hansen solubility parameter (HSP) sphere of NiO_x nanoparticles (NPs) simulated via HSPiP software. The small blue sphere inside the large green sphere indicates a good solvent for the dispersion of NiO_x NPs. The photograph shows NiO_x NPs highly dispersed in 1-hexanol. e–j) Top-view scanning electron microscopy (SEM) images of perovskite films with different NiO_x concentrations. Scale bar, 1 μm .

To experimentally demonstrate the sputtering damage for each condition, we measured cross-sectional SEM of the: i) perovskite/ITO; ii) perovskite/spiro-OMeTAD/ITO; and iii) perovskite/NiO_x/ITO structure, respectively. In the case of depositing ITO directly on the perovskite layer, the perovskite layer had collapsed due to sputtering damage (Figure S3a, Supporting Information). With spiro-OMeTAD on the perovskite layer, many voids in the spiro-OMeTAD layer are observed after ITO deposition in Figure S3b, Supporting Information, suggesting that the spiro-OMeTAD layer was damaged during the sputtering process. On the other hand, in the case of perovskite/NiO_x/ITO, the ITO electrode was well deposited without any damage to NiO_x and perovskite layers, which indicates

NiO_x layer prevents sputtering damage during the deposition of the ITO electrode (Figure S3c, Supporting Information). This result demonstrated the metal oxide CTL on top of the perovskite layer effectively prevents sputtering damage.

To further investigate whether the NiO_x layer prevents sputtering damage during the deposition of TTEs in a device, we fabricated planar n-i-p semi-transparent PSCs with a fluorine-doped tin oxide (FTO)/SnO₂/(FAPbI₃)_{0.95}(MAPbBr₃)_{0.05}/NiO_x/ITO structure (Figure 2a). As shown in Figure S3c, Supporting Information, we confirmed the thickness of the NiO_x layer was 54 nm. Figure 2b shows a photograph of the semi-transparent PSCs with ITO and ITO-Au finger electrodes (ITO-grid). Au finger electrode was deposited on the ITO electrode for

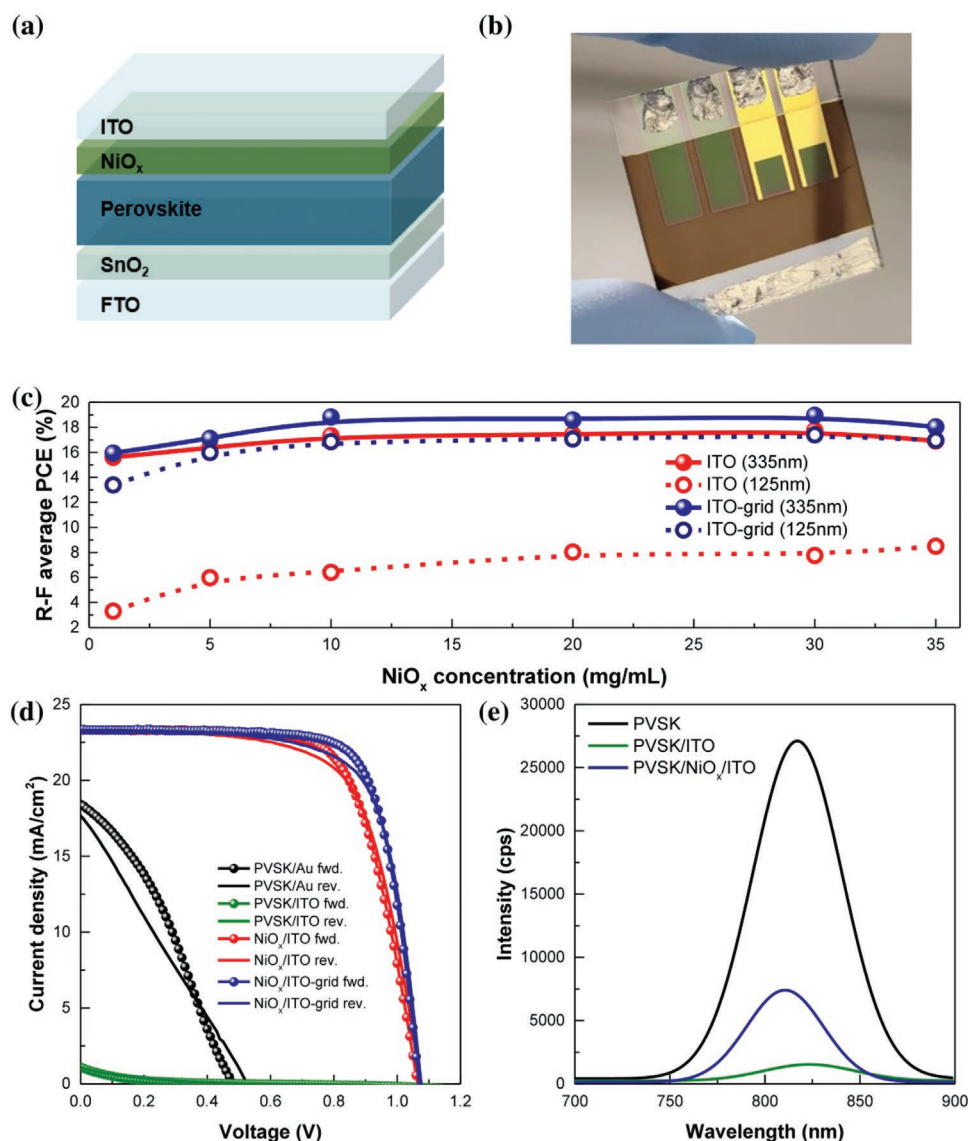


Figure 2. a) Configuration of the semi-transparent PSC with n-i-p structure. b) A photograph of a semi-transparent PSC with n-i-p structure. c) Power conversion efficiency (PCE) variation of semi-transparent PSCs with different NiO_x concentrations depending on ITO thickness. d) Current density–voltage (J – V) curves of devices with perovskite/Au, perovskite/ITO, perovskite/ NiO_x /Au, and perovskite/ NiO_x /ITO on SnO_2 substrate. The NiO_x concentration is 30 mg mL^{-1} . e) Photoluminescence (PL) spectra of perovskite, perovskite/ITO, and perovskite/ NiO_x /ITO films on a quartz substrate.

efficient charge collection by improving the electrical conductivity. Figure 2c shows the reverse–forward average PCE (R–F average PCE) variation of semi-transparent PSCs with different concentrations of NiO_x solution depending on ITO thickness of 125 and 335 nm. Among various concentrations of the NiO_x solutions, the semi-transparent PSC with 30 mg mL^{-1} of concentration exhibits the highest R–F average PCE regardless of ITO thickness. This result suggests that the PCE decreases as the series resistance increases above the optimal thickness with full-coverage. Especially with an ITO thickness of 125 nm, the semi-transparent PSCs with ITO and ITO-grid showed R–F average PCE of 7.76% and 17.40%, respectively, suggesting that the Au finger effectively improved charge collection. However, the PCEs of ITO and ITO-grid devices are similar at 325 nm-thick ITO because ITO is thick enough to have low sheet

resistance. Figures S4 and S5, Supporting Information, show current density–voltage (J – V) curves of semi-transparent PSCs with ITO and ITO-grid electrodes at the ITO thickness of 125 and 335 nm. As shown in Tables S1–S4, Supporting Information, corresponding with Figures S4 and S5, Supporting Information, the semi-transparent PSC with 30 mg mL^{-1} NiO_x solution exhibited the best photovoltaic properties. For the application of tandem solar cells, TTEs should be thin to transmit more light in the near-infrared (NIR) region.^[39] However, a thin TTE layer generally shows lower electrical conductivity, which deteriorates the photovoltaic properties of devices. In the case of the thin TTE layer, the metal finger electrode is required to improve the photovoltaic properties of devices. As shown in Figure 2c, at an ITO thickness of 125 nm, devices with ITO-grid showed a significantly enhanced R–F average PCE compared to devices

Table 1. Photovoltaic parameters of devices with perovskite/Au, perovskite/ITO, perovskite/ NiO_x /Au, and perovskite/ NiO_x /ITO on the SnO_2 substrate.

Devices	Scan direction	J_{sc} [mA cm^{-2}]	V_{oc} [V]	FF [%]	PCE [%]	R-F average PCE [%]
PVSK/Au	fwd.	18.42	0.48	33.71	2.98	2.65
	rev.	17.68	0.53	24.92	2.33	
PVSK/ITO	fwd.	1.11	0.52	8.96	0.05	0.06
	rev.	1.11	0.66	10.06	0.07	
PVSK/ NiO_x /ITO	fwd.	23.31	1.06	69.76	17.23	17.01
	rev.	23.26	1.07	67.46	16.79	
PVSK/ NiO_x /ITO-grid	fwd.	23.32	1.07	74.50	18.59	18.24
	rev.	23.31	1.08	71.08	17.89	

with ITO due to improved electrical conductivity. Therefore, ITO-grid-based devices with an ITO thickness of 125 nm are suitable for tandem solar cells, while the devices with an ITO thickness of 335 nm are suitable for highly efficient visible light semi-transparent PSCs without a metal finger grid.

To investigate sputtering damage to the perovskite layer, we additionally fabricated HTL-free devices with Au or ITO as a top electrode. Figure 2d shows J - V curves of HTL-free devices with Au or ITO as the top electrode and NiO_x -based devices with an ITO electrode. As shown in Table 1, the HTL-free device with Au showed a short-circuit current density (J_{sc}) of 18.42 mA cm^{-2} , open-circuit voltage (V_{oc}) of 0.48 V, fill factor (FF) of 33.71% and PCE of 3.0% under the forward scan direction, whereas the HTL-free device with ITO did not operate as a solar cell. This indicates that the direct deposition of ITO on the perovskite layer leads to significant degradation of the perovskite layer due to sputtering damage. In contrast, NiO_x -based device with an ITO electrode showed a J_{sc} of 23.31 mA cm^{-2} , V_{oc} of 1.06 V, FF of 69.76% and PCE of 17.2% under the forward scan direction, indicating that the NiO_x layer successfully prevents sputtering damage. To further elucidate the sputtering damage to the perovskite layer, we conducted steady-state photoluminescence (PL) analysis of perovskite, perovskite/ITO, and perovskite/ NiO_x /ITO films on quartz glass (Figure 2e). The perovskite/ITO film showed almost no PL intensity compared with that of the perovskite layer, whereas the perovskite/ NiO_x /ITO film showed a reduced PL intensity due to charge carrier quenching. These results demonstrate that the NiO_x layer not only effectively prevents sputtering damage without a buffer layer but also finely functions as an HTL.

To investigate sputtering damage in terms of organic HTLs, we fabricated opaque PSCs and semi-transparent PSCs using spiro-OMeTAD as an HTL. As shown in Figure S6 and Table S5, Supporting Information, the semi-transparent device based on spiro-OMeTAD showed significantly reduced photovoltaic parameters compared with those of the opaque device due to sputtering damage to the spiro-OMeTAD and perovskite layers. This result indicates that organic HTLs without buffer layers are not suitable for semi-transparent PSCs fabricated via the sputtering process.

To optimize ITO deposition conditions for high-performance semi-transparent PSCs, we prepared ITO films on quartz glass

with various sputtering powers. Figures S7 and S8, Supporting Information, show the optical transmittance and Hall measurement results for the ITO films fabricated with different sputtering power. The AVT values of ITO films fabricated with 50, 100, 150, 200, 250 or 300 W power are 85.63%, 84.30%, 84.09%, 86.23%, 83.19%, and 80.51% respectively. The AVT was defined as the region in wavelength between 430 and 675 nm.^[40,41] The sheet resistance and resistivity of the ITO films show a minimum at 200 W. To determine the optimal condition of ITO deposition power, we calculated the figure of merit values (FOM) according to “FOM = (AVT)¹⁰/sheet resistance”. Based on the calculated FOM values, we confirmed the sputtering power of 200 W as the optimal condition for ITO deposition power (Figure S9, Supporting Information). As a result, the semi-transparent device with ITO fabricated with 200 W showed better photovoltaic parameters than those fabricated under other conditions (Figure S10 and Table S6, Supporting Information). To investigate the effect of ITO deposition temperature on photovoltaic performance, we fabricated semi-transparent PSCs with different processing temperatures. As shown in Figure S11 and Table S7, Supporting Information, the semi-transparent PSCs exhibited similar PCE values up to 100 °C and a slightly decreased PCE at 125 °C. This result suggests that the NiO_x -based semi-transparent devices are durable under the ITO deposition temperature at 100 °C.

To further optimize ITO deposition conditions with respect to ITO thickness, we prepared ITO films with different thicknesses on quartz glass by controlling the deposition time. Figure 3a,b shows the optical transmittance and Hall measurement results of ITO films with different thicknesses. We confirmed that the AVT values of ITO films decreased over the thickness of 335 nm, and sheet resistance and resistivity decreased with increasing thickness except for 850 nm. We calculated the FOM of ITO films with different thicknesses to determine the optimal ITO deposition thickness. Based on the calculated FOM of ITO films, we found higher FOM values above the thickness of 229 nm. However, we observed similar FOM values above the thickness of 229 nm because optical transmittance and sheet resistance decreased with increasing the thickness. To investigate photovoltaic performance depending on ITO thickness, we fabricated semi-transparent PSCs with various thicknesses of ITO film. As shown in Figure 3c and Table 2, the device with an ITO thickness of 335 nm showed the highest PCE of 17.4% under the forward scan and an R-F average PCE of 17.1%. Therefore, the ITO thickness of 335 nm is suitable for high-performance semi-transparent PSCs.

Figure 3d shows the optical transmittance of semi-transparent PSCs with different thicknesses of the ITO electrode. The transmittance in the visible region was observed to be similar regardless of ITO thickness; however, high transmittance in the NIR region was observed with an ITO thickness of 125 nm. In order to visually show the transmittance as a function of the ITO thickness in the visible and NIR region, the integrated transmittance for each of the visible and NIR regions is represented in Figure 3e. As shown in Figure 3e, In the NIR region, a higher transmittance was observed as the ITO thickness decreased. Therefore, an ITO thickness of 125 nm is suitable for silicon-perovskite tandem solar cells where high transmittance is necessarily required. To experimentally

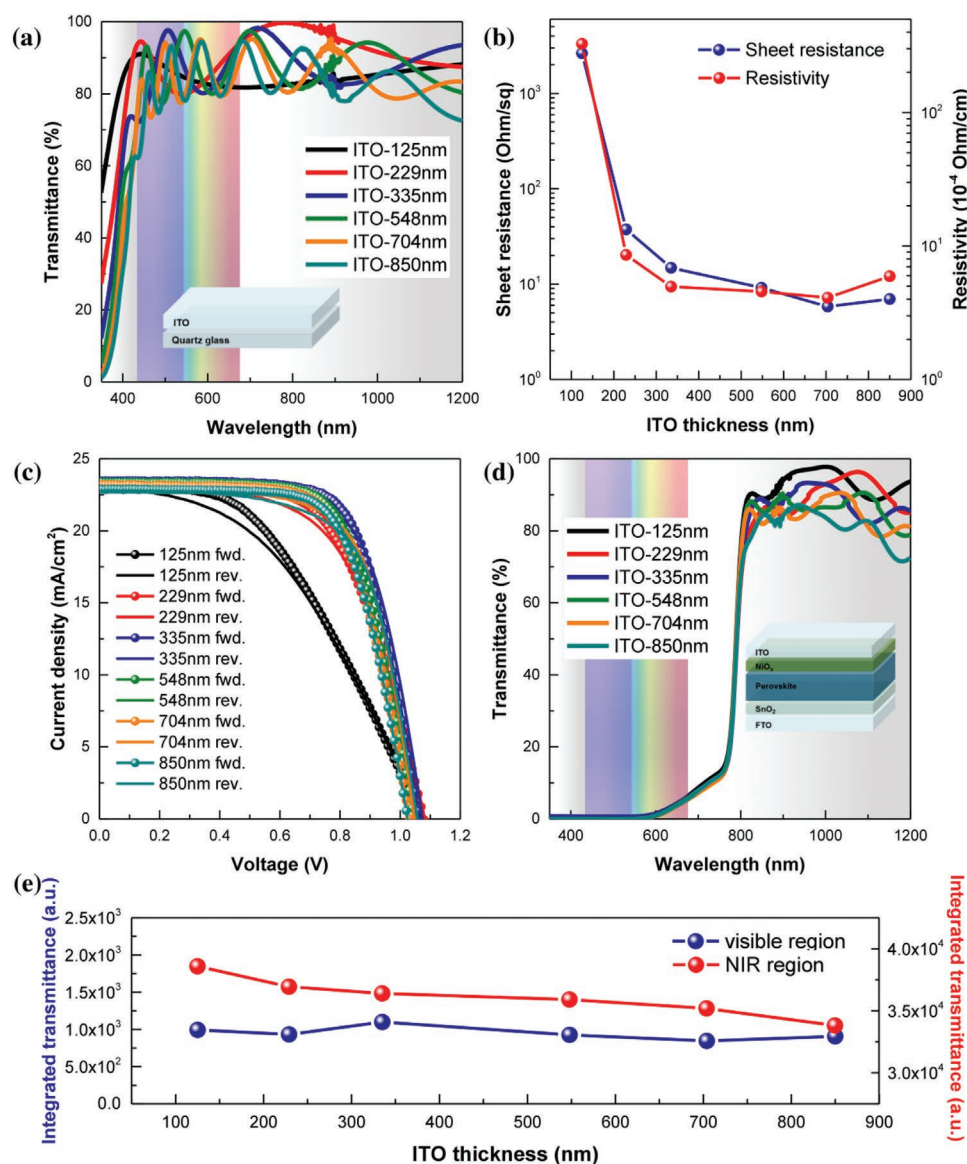


Figure 3. a) Optical transmittance of ITO films on a quartz substrate with different thicknesses of ITO electrode. b) Sheet resistance and resistivity of ITO films on a quartz substrate with different thicknesses of ITO electrode. c) J - V curves of semi-transparent PSCs based on NiO_x with different thicknesses of ITO without Au finger electrodes. d) Optical transmittance of semi-transparent PSC with different thicknesses of ITO electrode. e) Integration of transmittance of visible and NIR region with different thicknesses of ITO electrode.

demonstrate the optimal ITO thickness for silicon-perovskite tandem solar cells, we measured the silicon solar cell using semi-transparent PSC as UV and visible light filter, as shown in Figure S12a, Supporting Information. Since the semi-transparent PSC absorbs the region below 800 nm, the silicon solar cell mainly absorbs light in the NIR region. As shown in Figure S12b and Table S8, Supporting Information, the light filter significantly decreased J_{sc} of the silicon solar cell owing to the reduced transmittance in UV and visible regions. We confirmed J_{sc} of the silicon solar cell decreased as the ITO thickness increased, which is related to NIR transmittance of ITO. According to the previously reported literatures,^[42,43] the ITO thickness affects the J_{sc} of silicon solar cells in tandem structure. Therefore, the ITO thickness of 125 nm is more suitable

for silicon-perovskite tandem solar cells compared with a thick ITO electrode.

As a representative of the optimized semi-transparent PSCs architecture, a cross-sectional SEM image of the optimized device is shown in Figure 4a. Figure 4b shows the J - V curves of opaque and semi-transparent PSCs, which were optimized by controlling the thickness of the NiO_x layer and ITO deposition conditions, and all photovoltaic parameters are summarized in Table 3. The best-performing semi-transparent device with ITO-grid showed 19.48% efficiency with a J_{sc} of 23.33 mA cm^{-2} , a V_{oc} of 1.08 V, and FF of 77.28% under the forward scan direction. As shown in Table S9, Supporting Information, we confirmed that this work showed the highest PCE among organic layer-free semi-transparent PSCs reported so far. We excluded

Table 2. Photovoltaic parameters of semi-transparent PSCs based on NiO_x with different thicknesses of ITO electrode.

Devices	Scan direction	J_{sc} [mA cm^{-2}]	V_{oc} [V]	FF [%]	PCE [%]	R-F average PCE [%]
ITO-125 nm	fwd.	23.08	1.07	45.58	11.25	11.03
	rev.	22.93	1.07	44.08	10.81	
ITO-229 nm	fwd.	23.16	1.08	61.70	15.43	15.17
	rev.	22.98	1.08	60.06	14.91	
ITO-335 nm	fwd.	23.47	1.06	69.76	17.35	17.13
	rev.	23.42	1.07	67.46	16.90	
ITO-548 nm	fwd.	23.39	1.05	67.63	16.61	16.44
	rev.	23.09	1.05	67.06	16.26	
ITO-704 nm	fwd.	23.19	1.03	67.38	16.09	16.22
	rev.	23.08	1.05	67.49	16.35	
ITO-850 nm	fwd.	22.90	1.02	69.01	16.12	16.06
	rev.	22.79	1.06	66.30	16.01	

the literature containing the organic layer such as BCP and spiro-OMeTAD. Although the opaque device showed a higher J_{sc} due to light reflection at the Au electrode, the semi-transparent device showed higher PCE, which was attributed to enhanced V_{oc} and FF. It is noteworthy that semi-transparent PSCs are more efficient than opaque PSCs. This result suggests that NiO_x based PSCs with the n-i-p structure are ideal candidates for highly efficient semi-transparent PSCs.

To investigate the improved photovoltaic performance of semi-transparent devices compared to opaque devices, we carried out Mott-Schottky analysis at 10 kHz under dark conditions to estimate the flat-band potentials (V_{FB}) (Figure S13a, Supporting Information). A V_{FB} of 1.06 V for the semi-transparent device is higher than a V_{FB} of 1.01 V for the opaque device, resulting in an improved V_{oc} . Furthermore, we measured the dark current density and V_{oc} with light intensity of semi-transparent and opaque devices. As shown in Figure S13b, Supporting Information, the semi-transparent device showed a reduced leakage current density compared to the opaque device. Figure S13c, Supporting Information, represents the linear plot of V_{oc} as a function of the light intensity according to " $V_{oc} = n_{id}(k_B T/q) \ln(\text{light intensity}) + a$ " equation, where n_{id} , k_B , T , q and a are ideality factor, Boltzmann constant, temperature, elementary charge and constant. We confirmed an n_{id} of 1.13 for semi-transparent device is lower than an n_{id} of 1.53 opaque device, indicating that the NiO_x/ITO contact is better than NiO_x/Au contact. As previously reported, additional annealing is required to improve interface contact between NiO_x and Au layer due to the poor interface contact.^[44] Therefore, we speculate that the higher V_{oc} and FF for ITO are attributed to an improved interface contact.

To investigate the work function matching of the semi-transparent device, we measured ultraviolet photoelectron spectroscopy (UPS) spectra in Figure S14a, Supporting Information. Figure S14b, Supporting Information, shows the energy band diagram of the semi-transparent device, which is calculated from the UPS results and previously reported literatures.^[38,45] As shown in Figure S14b, Supporting Information, the valence

band level of NiO_x is well matched for efficient hole transport between the perovskite and ITO layer. To elucidate the carrier injection depending on electrodes, we conducted time-correlated single-photon counting (TCSPC) analysis of the perovskite, perovskite/ NiO_x , perovskite/ NiO_x/ITO , and perovskite/ NiO_x/Au , respectively. As shown in Figure S15, Supporting Information, the condition of perovskite/ NiO_x/ITO shows more efficient hole transport than the perovskite/ NiO_x/Au , which is related to the improved interface contact.

To verify the measured J_{sc} of the opaque and semi-transparent PSCs, we conducted external quantum efficiency (EQE) measurements (Figure 4c). The integrated J_{sc} s of the Au, ITO and ITO-grid devices were calculated to be 24.35, 23.02 and 23.14 mA cm^{-2} , showing the small deviation from J_{sc} s obtained from J - V curves, respectively. Figure 4d shows the optical transmittance of opaque and semi-transparent PSCs. We confirmed that the semi-transparent device showed transmittance in the visible and NIR regions, whereas the opaque device with the Au electrode showed zero transmittance overall in wavelengths. We conducted the storage stability test of semi-transparent PSCs under 10% relative humidity at room temperature without encapsulation (Figure 4e). The semi-transparent devices showed superior storage stability regardless of Au finger electrode, retaining over 90% of the initial PCE for 1000 h.

Figure 5a shows J - V curves of the ITO-grid device according to light illumination direction and in the presence of the mirror as a back reflector. As shown in Table 4, the ITO-grid device showed an R-F average PCE of 18.2% under bottom-side FTO illumination and 11.94% under top-side ITO illumination. With a back reflector, the ITO-grid showed an improved PCE of 20.5%, which is attributed to enhanced J_{sc} and V_{oc} due to the reflected light at the mirror side. Figure 5b shows the EQE spectra of the ITO-grid device according to illumination direction. We observed that the EQE spectrum of the ITO-grid device under top-side ITO illumination was recorded to be lower over the entire wavelength than that under bottom-side FTO illumination. The large difference in the EQE spectrum is attributed to the large transmittance of the FTO/ SnO_2 side relative to that of NiO_x/ITO side. The integrated J_{sc} of the ITO-grid device was 23.08 mA cm^{-2} under bottom-side FTO illumination and 18.51 mA cm^{-2} under top-side ITO illumination.

To maximize the transmittance of semi-transparent PSCs, we controlled the molar concentration of the perovskite precursor solution to fabricate a thinner active layer, which can transmit more light. Figure 5c shows the J - V curves of the semi-transparent PSCs with different molar concentrations of the perovskite precursor solution. As the molar concentration decreases, the J_{sc} decreases due to the thinner active layer, resulting in lower PCE, as shown in Table 5. Figure 5d shows the optical transmittance of semi-transparent PSCs with different molar concentrations of the perovskite precursor solution. The 0.5, 1.0 and 1.4 M conditions exhibited the AVT of 30.31%, 7.29% and 1.99%, respectively.

To further investigate the optimal condition for semi-transparent PSCs, we calculated the light use efficiency (LUE) values from different molar concentration conditions according to " $\text{LUE} = \text{AVT} \times \text{PCE}$ ".^[18] Based on the calculated LUE results, the 0.5 M condition is the optimal condition for semi-transparent PSCs, showing the highest LUE of 375.23×10^{-4} .

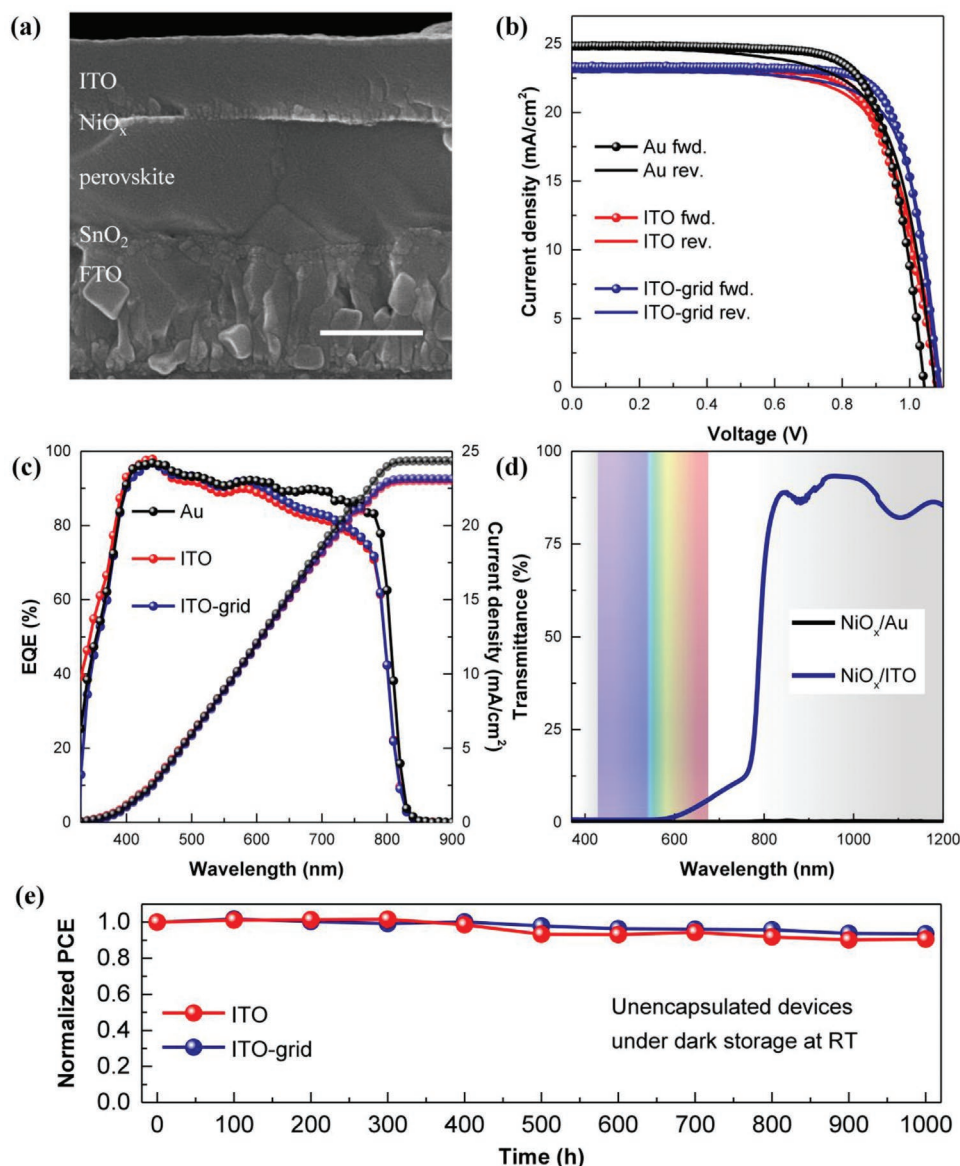


Figure 4. a) Representative cross-sectional SEM images of the semi-transparent n-i-p PSC based on NiO_x as an HTL. Scale bar, 500 nm. b) J - V curves of PSCs based on NiO_x with different top electrode. c) EQE spectra and the integrated J_{sc} of the corresponding perovskite solar cells. d) Optical transmittance of semi-transparent PSCs with different top electrodes. e) Storage stability of transmittance of semi-transparent PSCs based on NiO_x as a function of time.

Table 3. Photovoltaic parameters of PSCs based on NiO_x with a different top electrode.

Devices	Scan direction	J_{sc} [mA cm^{-2}]	V_{oc} [V]	FF [%]	PCE [%]	R-F average PCE [%]
Au	fwd.	24.82	1.04	74.26	19.17	18.73
	rev.	24.68	1.07	69.24	18.28	
ITO	fwd.	23.27	1.08	71.69	18.02	17.76
	rev.	22.96	1.09	69.86	17.49	
ITO-grid	fwd.	23.33	1.08	77.28	19.48	18.96
	rev.	22.97	1.09	73.63	18.44	

Figure 5e–g shows the photographs of semi-transparent PSCs with different molar concentrations of the perovskite precursor solution. At 0.5 M condition, we are able to clearly observe the building behind the semi-transparent device. This result suggests that the NiO_x based semi-transparent PSCs with n-i-p structure have great potential for BIPV applications.

3. Conclusion

In this study, we report an optimal architecture with oxide/perovskite halide/oxide for the high performance and commercialization of semi-transparent PSCs. We successfully

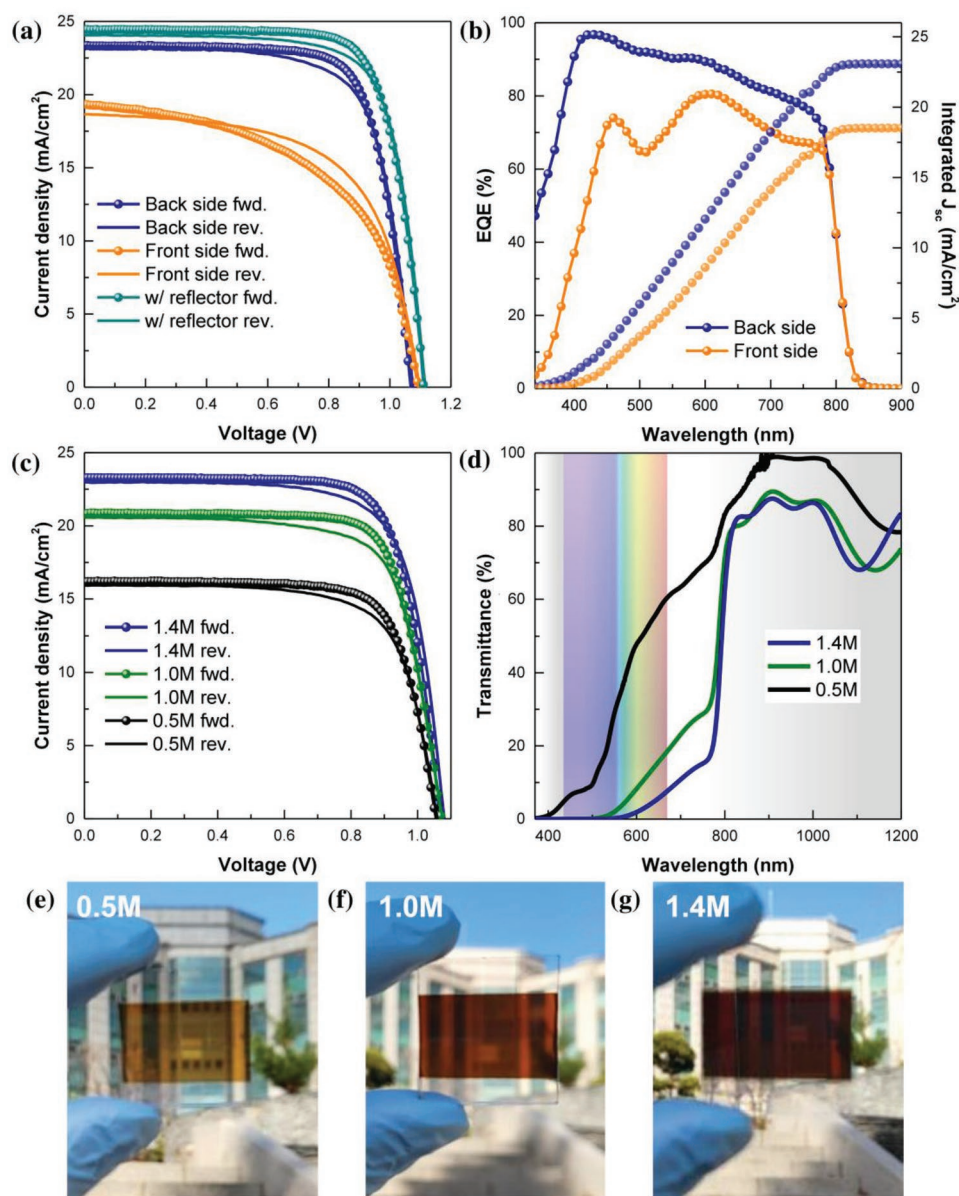


Figure 5. a) J - V curves of semi-transparent PSCs based on NiO_x according to illumination direction and with mirror on bottom side. b) EQE of semi-transparent PSCs based on NiO_x according to illumination direction and with mirror on bottom side. c) J - V curves and d) optical transmittance of semi-transparent PSCs based on NiO_x with different molar concentrations of the perovskite solution. e–g) Photographs of semi-transparent PSCs with different concentrations of the perovskite solution.

Table 4. Photovoltaic parameters of semi-transparent PSCs based on NiO_x according to illumination direction and with mirror.

Devices	Scan direction	J_{sc} [mA cm^{-2}]	V_{oc} [V]	FF [%]	PCE [%]	R–F average PCE [%]
Bottom FTO side	fwd.	23.32	1.07	74.50	18.59	18.24
	rev.	23.31	1.08	71.08	17.89	
Top ITO side	fwd.	19.34	1.09	53.63	11.31	11.94
	rev.	18.64	1.10	61.26	12.56	
With reflector	fwd.	24.45	1.11	75.48	20.48	20.20
	rev.	24.05	1.12	73.90	19.91	

demonstrated the sputtering damage-free semi-transparent PSCs by introducing the NiO_x as an overlayer on the perovskite, preventing the sputtering damage under harsh deposition conditions. The NiO_x based semi-transparent devices showed an improved PCE of 19.5% (20.48% with a back reflector) compared with the opaque devices due to the enhanced V_{oc} and FF. Furthermore, we controlled the molar concentration of the perovskite solution to maximize the transmittance of devices. As a result, we were able to fabricate semi-transparent PSCs with a high AVT of 30.31%, which is suitable for BIPV applications. We believe this work will be the cornerstone for the high performance and commercialization of semi-transparent PSCs.

Table 5. Photovoltaic parameters of semi-transparent PSCs based on NiO_x with different perovskite molar concentrations.

Devices	Scan direction	J_{sc} [mA cm^{-2}]	V_{oc} [V]	FF [%]	PCE [%]	R-F average PCE [%]
0.5 M	fwd.	16.19	1.06	74.36	12.76	12.38
	rev.	15.93	1.06	71.03	12.00	
1.0 M	fwd.	20.84	1.07	75.46	16.83	16.36
	rev.	20.57	1.07	72.18	15.89	
1.4 M	fwd.	23.29	1.07	74.89	18.66	18.37
	rev.	22.98	1.08	72.81	18.07	

4. Experimental Section

Materials: Methyl ammonium chloride, tin(II) chloride dihydrate, urea, mercaptoacetic acid, sodium acetate, nickel(II) acetylacetonate, 1-hexanol, *N,N*-dimethylformamide, and dimethyl sulfoxide were purchased from Sigma Aldrich. Formamidinium iodide was purchased from Alfa Aesar. Lead iodide, lead bromide, methyl ammonium bromide, and formamidinium iodide purchased from Tokyo Chemical Industry Co. 2,2',7,7'-tetrakis (*N,N*-di-4-methoxyphenylamine)-9,9'-spirobifluorene (spiro-OMeTAD) was purchased from Lumtec. All chemicals were used without further purification.

Synthesis of Ligand-Off NiO_x NPs: 2 mmol of nickel (II) acetylacetonate was dissolved in a mixed solution of 20 mL oleylamine and 20 mL toluene under magnetic stirring. After stirring for few minutes, it becomes a dark blue solution. Then the solution was put into a heating oven at a temperature of 180 °C and kept for 24 h. The solution was cooled down to room temperature and clear green solution was obtained. Afterward, acetone was poured into the solution and centrifuged to precipitate the synthesized NiO_x NPs. The precipitation was thoroughly washed with ethanol and methanol several times to remove the oleylamine ligands and unwanted by-chemicals. The obtained NiO_x NPs powder was dried at 70 °C for 1 h and then dispersed in 1-hexanol with different concentrations for further experiments.

Device Fabrication: FTO substrates (Asahi glass) were chemically etched using a zinc powder and HCl solution (concentrated hydrochloric acid: water = 1:3.5 v/v). The etched substrates were sequentially washed with detergent, water, and isopropanol. After drying the substrates, all substrates were treated with UV-ozone for 30 min before tin oxide (SnO_2) deposition. The SnO_2 layer was prepared by the chemical bath deposition method according to previously reported literature.^[8] A solution for the perovskite precursor was prepared by dissolving 569 mg mL^{-1} of lead iodide, 212 mg mL^{-1} of formamidinium iodide, 31 mg mL^{-1} methylammonium lead bromide, and 25 mg mL^{-1} methyl ammonium chloride in *N,N*-dimethylformamide:dimethyl sulfoxide (8:1 v/v) mixed solvent. Then, the precursor solution was spin-coated on a SnO_2 /FTO substrate at a spin rate of 1000 rpm and 5000 rpm for 5 and 15 s, respectively. During the second step, 1 mL of diethyl ether was quickly dropped on the substrate. The intermediate film substrate was annealed on a 150 °C hot plate for 10 min. The NiO_x nanoparticles were synthesized referring to previously reported literature.^[38] NiO_x nanoparticle colloidal solution was spin-coated on the perovskite layer at 2000 rpm for 30 s. After deposition of the NiO_x layer, the film was annealed at 120 °C for 10 min. Finally, a 110 nm thick Au electrode was deposited by thermal evaporation at a pressure of 9×10^{-6} Torr. In case of ITO-grid electrode, the Au finger on ITO is fabricated with the same fabrication method as fabricate Au electrode except for the metal mask. A metal mask for ITO-grid was designed to be deposited on the edge of the active area of the ITO electrode.

Characterization: *J*-*V* curves were measured using a solar simulator (Newport, Oriel Class A, 91195A) with a source meter (Keithley 2420) under illumination at AM 1.5G, which was calibrated using a Si-reference cell certificated by NREL. For the *J*-*V* curve characterization, the step voltage and scan speed were fixed at 10 mV and 100 mV s^{-1} , respectively. For the measurement of high-performance devices, an anti-reflecting coating was

conducted on the surface. The EQE was measured using a QUANTX-300 QE measurement with a 100W xenon lamp source and 130 mm focal length monochromator with dual gratings. The morphology of the films was measured using a scanning electron microscope (Quanta 250 FEG). Optical properties of films were measured using UV-Vis spectroscopy (Cary 5000, Agilent Technologies). UPS spectra were obtained using a Sigam Probe (Thermo VG Scientific) under ultra-high vacuum. The steady-state photoluminescence was measured using a 485 nm diode laser (Horiba, DeltaDiode-485L) with a repetition rate of 25 MHz. A liquid-nitrogen-cooled low noise photomultiplier tube (Hamamatsu, R5509-43) with a 500 nm longpass filter was used to collect emission photons from the specimens. Time-correlated single photon counting (TCSPC) was carried out using the pulsed mode of the diode laser with 485 nm (Horiba, DeltaDiode-485L-CW). The photon for the film was collected using the double-grating monochromator (Horiba, FL-1005) and a liquid-nitrogen-cooled low noise photomultiplier tube (Hamamatsu, R5509-43). A 500 nm long-pass filter was used to remove the signal from the source laser.

Supporting Information

Supporting Information is available from the Wiley Online Library or from the author.

Acknowledgements

This work was supported by the National Research Foundation of Korea grant by the Korea government (MSIO) (NRF-2020R1A2C3009115 and NRF-2020R1A4A2002161) and the New and Renewable Energy Core Program of the Korea Institute of Energy Technology Evaluation and Planning (KETEP) from the Ministry of Trade, Industry, and Energy (20183010014470). This work was also supported by a grant from Hyundai Motor Company (R-204696).

Conflict of Interest

The authors declare no conflict of interest.

Author Contributions

M.J.J. and J.H.L. contributed equally to this work. M.J.J., J.H.L., and J.H.N. conceived the work and designed the experiment. J.H.L., C.H.Y., and M.J.J. performed the fabrication and characterization of the semi-transparent PSCs with various conditions. J.H.L. and C.H.Y. conducted the UV-VIS measurement of ITO films and devices. S.Y.K. and S.L. carried out the Hall measurement of ITO films. M.J.J. and J.H.N. wrote the manuscript reflecting the feedbacks and comments of all authors. J.H.N. directed and supervised this project.

Data Availability Statement

The data that support the findings of this study are available from the corresponding author upon reasonable request.

Keywords

oxide overlayers, perovskite solar cells, semi-transparent, sputtering damage-free

Received: February 25, 2022

Revised: May 31, 2022

Published online:

- [1] K. Lee, H. D. Um, D. Choi, J. Park, N. Kim, H. Kim, K. Seo, *Cell Rep. Phys. Sci.* **2020**, 1, 100143.
- [2] S. Rahmany, L. Etgar, *ACS Energy Lett.* **2020**, 5, 1519.
- [3] C. D. Bailie, M. G. Christoforo, J. P. Mailoa, A. R. Bowring, E. L. Unger, W. H. Nguyen, J. Burschka, N. Pellet, J. Z. Lee, M. Grätzel, R. Noufi, T. Buonassisi, A. Salleo, M. D. McGehee, *Energy Environ. Sci.* **2015**, 8, 956.
- [4] N. G. Park, *Mater. Today* **2015**, 18, 65.
- [5] J. H. Noh, S. H. Im, J. H. Heo, T. N. Mandal, S. I. Seok, *Nano Lett.* **2013**, 13, 1764.
- [6] J. Y. Kim, J. W. Lee, H. S. Jung, H. Shin, N. G. Park, *Chem. Rev.* **2020**, 120, 7867.
- [7] B. Shi, L. Duan, Y. Zhao, J. Luo, X. Zhang, *Adv. Mater.* **2020**, 32, 1806474.
- [8] J. J. Yoo, G. Seo, M. R. Chua, T. G. Park, Y. Lu, F. Rotermund, Y. K. Kim, C. S. Moon, N. J. Jeon, J. P. Correa-Baena, V. Bulović, S. S. Shin, M. G. Bawendi, J. Seo, *Nature* **2021**, 590, 587.
- [9] J. Jeong, M. Kim, J. Seo, H. Lu, P. Ahlawat, A. Mishra, Y. Yang, M. A. Hope, F. T. Eickemeyer, M. Kim, Y. J. Yoon, I. W. Choi, B. P. Darwich, S. J. Choi, Y. Jo, J. H. Lee, B. Walker, S. M. Zakeeruddin, L. Emsley, U. Rothlisberger, A. Hagfeldt, D. S. Kim, M. Grätzel, J. Y. Kim, *Nature* **2021**, 592, 381.
- [10] Y. Y. Kim, T. Y. Yang, R. Suhonen, A. Kemppainen, K. Hwang, N. J. Jeon, J. Seo, *Nat. Commun.* **2020**, 11, 5146.
- [11] N. G. Park, K. Zhu, *Nat. Rev. Mater.* **2020**, 5, 333.
- [12] Q. Jiang, Y. Zhao, X. Zhang, X. Yang, Y. Chen, Z. Chu, Q. Ye, X. Li, Z. Yin, J. You, *Nat. Photonics* **2019**, 13, 460.
- [13] D. K. Lee, D. N. Jeong, T. K. Ahn, N. G. Park, *ACS Energy Lett.* **2019**, 4, 2393.
- [14] E. H. Jung, N. J. Jeon, E. Y. Park, C. S. Moon, T. J. Shin, T. Y. Yang, J. H. Noh, J. Seo, *Nature* **2019**, 567, 511.
- [15] S. Lee, K. Choi, C. H. Min, M. Y. Woo, J. H. Noh, *MRS Bull.* **2020**, 45, 439.
- [16] P. Zhu, S. Gu, X. Luo, Y. Gao, S. Li, J. Zhu, H. Tan, *Adv. Energy Mater.* **2020**, 10, 1903083.
- [17] E. J. López-Naranjo, L. J. González-Ortiz, L. M. Apátiga, E. M. Rivera-Muñoz, A. Manzano-Ramírez, *J. Nanomater.* **2016**, 2016, 4928365.
- [18] S. H. Lim, H. J. Seok, M. J. Kwak, D. H. Choi, S. K. Kim, D. H. Kim, H. K. Kim, *Nano Energy* **2021**, 82, 105703.
- [19] Z. Ying, X. Yang, J. Zheng, Y. Zhu, J. Xiu, W. Chen, C. Shou, J. Sheng, Y. Zeng, B. Yan, H. Pan, J. Ye, Z. He, *J. Mater. Chem. A* **2021**, 9, 12009.
- [20] Z. Wei, B. Smith, F. De Rossi, J. R. Searle, D. A. Worsley, T. M. Watson, *J. Mater. Chem. C* **2019**, 7, 10981.
- [21] F. Liang, Z. Ying, Y. Lin, B. Tu, Z. Zhang, Y. Zhu, H. Pan, H. Li, L. Luo, O. Ageev, Z. He, *Adv. Mater. Interfaces* **2020**, 7, 2000591.
- [22] D. Chen, S. Pang, L. Zhou, X. Li, A. Su, W. Zhu, J. Chang, J. Zhang, C. Zhang, Y. Hao, *J. Mater. Chem. A* **2019**, 7, 15156.
- [23] H. Jung, G. Kim, G. S. Jang, J. Lim, M. Kim, C. S. Moon, X. Hao, N. J. Jeon, J. S. Yun, H. H. Park, J. Seo, *ACS Appl. Mater. Interfaces* **2021**, 13, 30497.
- [24] Y. J. Noh, J. G. Kim, S. S. Kim, H. K. Kim, S. I. Na, *J. Power Sources* **2019**, 437, 226894.
- [25] J. C. Yu, J. Sun, N. Chandrasekaran, C. J. Dunn, A. S. R. Chesman, J. J. Jasieniak, *Nano Energy* **2020**, 71, 104635.
- [26] W. Cao, J. Li, H. Chen, J. Xue, *J. Photonics Energy* **2014**, 4, 040990.
- [27] J. G. Kim, J. H. Lee, S. I. Na, H. H. Lee, Y. Kim, H. K. Kim, *Org. Electron.* **2020**, 78, 105560.
- [28] W. C. Lai, K. W. Lin, T. F. Guo, P. Chen, Y. Y. Liao, *AIP Adv.* **2018**, 8, 015109.
- [29] Y. Mo, J. Shi, P. Zhou, S. Li, T. Bu, Y. B. Cheng, F. Huang, *Sol. RRL* **2019**, 3, 1900209.
- [30] M. Y. Woo, K. Choi, J. H. Lee, S. Y. Park, J. H. Noh, *Adv. Energy Mater.* **2021**, 11, 2003119.
- [31] S. Zhu, X. Yao, Q. Ren, C. Zheng, S. Li, Y. Tong, B. Shi, S. Guo, L. Fan, H. Ren, C. Wei, B. Li, Y. Ding, Q. Huang, Y. Li, Y. Zhao, X. Zhang, *Nano Energy* **2018**, 45, 280.
- [32] J. Werner, C. H. Weng, A. Walter, L. Fesquet, J. P. Seif, S. De Wolf, B. Niesen, C. Ballif, *J. Phys. Chem. Lett.* **2016**, 7, 161.
- [33] J. Werner, J. Geissbühler, A. Dabirian, S. Nicolay, M. Morales-Masis, S. De Wolf, B. Niesen, C. Ballif, *ACS Appl. Mater. Interfaces* **2016**, 8, 17260.
- [34] N. N. Lal, Y. Dkhissi, W. Li, Q. Hou, Y. B. Cheng, U. Bach, *Adv. Energy Mater.* **2017**, 7, 1602761.
- [35] T. Zhang, C. Y. Lee, Y. Wan, S. Lim, B. Hoex, *J. Appl. Phys.* **2018**, 124, 073106.
- [36] H. Kanda, A. Uzum, A. K. Baranwal, T. A. Nirmal Peiris, T. Uneyama, H. Imahori, H. Segawa, T. Miyasaka, S. Ito, *J. Phys. Chem. C* **2016**, 120, 28441.
- [37] S. Y. Park, S. J. Kim, J. H. Lee, M. J. Jeong, J. M. Lee, H. S. Jung, J. H. Noh, *Adv. Funct. Mater.* **2021**, 31, 2100863.
- [38] K. M. Yeom, S. U. Kim, M. Y. Woo, J. H. Noh, S. H. Im, *Adv. Mater.* **2020**, 32, 2002228.
- [39] J. He, E. Bi, W. Tang, Y. Wang, Z. Zhou, X. Yang, H. Chen, L. Han, *Sol. RRL* **2018**, 2, 1800004.
- [40] G. E. Eperon, V. M. Burlakov, A. Goriely, H. J. Snaith, *ACS Nano* **2014**, 8, 591.
- [41] L. Yuan, Z. Wang, R. Duan, P. Huang, K. Zhang, Q. Chen, N. K. Allam, Y. Zhou, B. Song, Y. Li, *J. Mater. Chem. A* **2018**, 6, 19696.
- [42] M. Jaysankar, W. Qiu, M. van Eerden, T. Aernouts, R. Gehlhaar, M. Debucquoy, U. W. Paetzold, J. Poortmans, *Adv. Energy Mater.* **2017**, 7, 1602807.
- [43] F. J. Ramos, S. Jutteau, J. Posada, A. Bercegol, A. Rebai, T. Guillemot, R. Bodeux, N. Schneider, N. Loones, D. Ory, C. Broussillou, G. Goaer, L. Lombez, J. Rousset, *Sci. Rep.* **2018**, 8, 16139.
- [44] G. Sheng, J. Wang, X. Xiao, X. Cai, X. Wang, Z. Bi, Y. Lu, Y. Liu, Y. Zhu, X. Xu, G. Xu, *Adv. Eng. Mater.* **2021**, 24, 2100962.
- [45] Y. Lee, S. Paek, K. T. Cho, E. Oveisi, P. Gao, S. Lee, J. S. Park, Y. Zhang, R. Humphry-Baker, A. M. Asiri, M. K. Nazeeruddin, *J. Mater. Chem. A* **2017**, 5, 12729.